Topology optimization of fluid flow using local thermal objective function based on field synergy principle

David Marti, Pierre-Henri Cocquet, Delphine Ramalingom, Alain Bastide

Topology optimization of fluid flow using local thermal objective function based on field synergy principle

David Marti[a], Pierre-Henri Cocquet[b], Delphine Ramalingom[a], Alain Bastide[a]

[a] *Physique et Ingénierie Mathématique pour l'énergie et l'Environnement (PIMENT), Université de la Réunion, 2 rue Joseph Wetzell, 97490, Sainte-Clotilde, France*
[b] *Laboratoire des Sciences pour l'Ingénieur Appliquées à la Mécanique et au génie Électrique (SIAME), Université de Pau et des Pays de l'Adour, E2S UPPA, Pau, France*

Abstract

Topology optimization is widely used to design heat exchangers and may involve different expressions of objective functions to increase heat exchange. This work proposes a new thermal objective function based on the local orientation of velocity and temperature gradient fields. The latter is then defined as the cosine of these two vector fields and thus our approach has connections with the field synergy principle. The cosine objective function is compared with a more classical one in a multi-objective optimization framework whose resolution is done with the adjoint method. Our results reveal that the cosine objective function lead to results that are comparable with those obtained with the classical cost function and may be used by designers to look for optimized design by taking into account the synergy of the fields. A study of the field synergy principle reveals that it is only an accurate indicator of heat exchange in some cases discussed in this article.

Keywords: Topology optimization, natural convection, objective function, adjoint sensitivity analysis, field synergy principle

1. Introduction

Thermal systems involving energy transfer and fluid flow are essential components in numerous industries such as civil engineering, aeronautics, spatial, transport, chemicals industry or mechanical industry. These thermal systems comprise specific components like pumps, compressors, heat exchangers, ducts and related devices. If a thermal system meets all the requirements and performs as expected during the design process, it can be manufactured efficiently. However, due to the need for more and more efficient thermal systems, optimizing the existing systems to find an "optimal" design in terms of some predefined criteria has become essential. From a physics perspective, the ideas to increase

*Corresponding author: David.Marti@univ-reunion.fr

the heat exchanged through a domain are [1]: (a) mixing the main flow and near wall flow; (b) reducing the boundary layer thermal thickness ; (c) generating vortex or secondary flow ; (d) raising the turbulence intensity. This heat exchange enhancement often decreases the mechanical performance of the flow through the domain. These principles have been (and are still) considered and applied for designing more efficient thermal systems. Over the years, different computational optimization design techniques have been proposed to optimize flow and thermal components. Among them, from the world of structural mechanics, came parametric optimization, shape optimization, and then topology optimization. Topology optimization aims to go beyond the designer's intuition and provide the shape that best suits the physical goals the designer prescribes. The resulting design can take any shape or topology from a geometrical point of view. Topology optimization in fluid mechanics started with [2] and have been applied to many types of flow as (for extensive reviews, see [3, 4]) steady laminar flow, unsteady flow, turbulent flow, non-Newtonian fluids, and for different kind of physics as conjugate heat transfer, fluid-structure interaction, microstructure in porous media. Different modes of heat transfer were studied: forced convection by [5, 6] and natural convection by [7].

In the field of topology optimization, several objective functions related to thermal exchanges are used to suit the need of the designer. The thermal performance of a thermal system can be evaluated by considering the following objective functions: maximize the thermal energy exchange of a fluid system using the quantities defined at the boundaries [8, 9, 10, 11], maximize recoverable thermal power [12], minimize thermal compliance [7, 13, 14, 6], maximize averaging temperature on the boundary [15], minimize mean temperature [16, 17, 18, 5, 16], minimize capacity dissipation [15], maximize heat generation [19, 20], minimize thermal resistance [21], minimize entropy generations [22, 23].

Each of the previous objective functions arises from different quantities derived from different insights of continuum mechanics and thermodynamics. In order to enhance thermal exchange, the current paper proposes a new objective function based on local observations of physic fields inside a studied domain. Based on physical justification, the local angle between the local velocity vector and the local temperature gradient vector will be used to create an objective function involving their cosine $\cos(\angle[\boldsymbol{u}, \nabla\theta])$ to encourage the whole flow to be in the same direction as the heat flux. Mathematically, that means the cosine will be close to 1 in the main flow. This approach can be linked to the *field synergy principle* (FSP) proposed by [24], where it is argued that the heat exchange in convection is increased when the velocity field of the flow tends to be in the same direction as the vector field of the temperature gradient. Since the field synergy is directly measured by the average of the mean angle formed by the velocity field and the temperature gradient over the domain [25], the constructed cosine objective function, which involves the summation of the cosine $\cos(\angle[\boldsymbol{u}, \nabla\theta])$ over the domain, complies with the FSP.
Bejan has criticized the FSP concept in [26], which states that this concept cannot be useful in a whole flow domain since heat exchanges arise mainly near heated boundaries. This has been acknowledge by [27], which shows that for

better results, the field synergy should be evaluated only within the thermal boundary. The FSP principle also shows some limitations with turbulent flow [28]. It would therefore be interesting to ask ourselves about the limits of our objective function and to consider them in the light of the literature on the subject. Still, the working group of the original authors produced answers, reviews and explanations [28, 29] citing various applications of this concept on successful optimization of various thermal devices. The applications studied with an analysis of the FSP cover multiple domains such as heat exchangers, fuel cells, porous medium, friction resistance reduction, solar energy receivers, vortex generator and diesel particulate filter. Most articles use classical optimization techniques, and compare then the field synergy before and after optimization with the conclusion that enhanced thermal performance led to a better synergy between flow and heat transfer. For example, in [15], thins added to a latent heat storage device thanks to topology optimization technique led to a performance gain of 80% and synergy fields ($\angle[\boldsymbol{u}, \nabla\theta]$) tend near 0 to 10 ° while it was near 175° before optimization. For finned tube banks heat exchangers, the articles [30, 31, 32] show that heat transfer performance increase is linked to the field synergy increase. In [33], the authors showed that optimizing the performance of a pre-heater in a solar-assisted desalination unit by 23% boosts the field synergy of 36%. In [34], it is shown that the best heat exchanger design through double-layered micro-channels with cavities and rib also had a better field synergy. In the current paper, we influence the synergy field directly by use of topology optimization problem considering an objective function linked to the FSP. To the best of our knowledge, this the first attempt to apply the FSP concept to topology optimization.

The current paper is organized as follows: Section 2 presents the studied physical problem and its modeling. Section 3 explains the construction of the cosine objective function. Section 4 demonstrates the derivation of the adjoint solver and its numerical implementation. Section 5 illustrates the newly defined objective function on two studied cases of the literature (the single and bend pipe), a comparison with the classical approach and a confrontation with the FSP principle. Lastly, Section 6 offers the conclusion.

2. Modelling

The topology optimization method used herein is based on the classical density approach proposed first for computational fluid mechanics by Borrvall and Petersson [2]. The working domain is characterized by a scalar field α (called the design variable) representing the pseudo-permeability of the fluid. This field penalizes the flow equations thanks to some term $h_\tau(\alpha)\boldsymbol{u}$ which makes them similar to a Brinkman-type model of Darcy's law for flow through a porous medium [3]. Equations (2)-(3) given below then describe a fluid if $h_\tau(\alpha)$ is zero and a solid if $h_\tau(\alpha)$ is large enough since, in that case, the velocity of the fluid in these zones is close to zero. The localization of the fluid-solid zones can then be done thanks to $h_\tau(\alpha)$ by using α as optimization parameter. The conductivity of the matter (fluid, solid) is also adjusted via the term k_τ. This formalism allows

studying heat exchange between fluid and solid with a single unified approach, unlike the classical conjugate heat transfer approach, where different physics are solved for the solid and flow parts.

The flow considered in this paper is incompressible, Newtonian, laminar and stable. The physics of the flow is described by the non-dimensional equations (1),(2),(3),(4) given below with the notation $\nabla_n = \boldsymbol{n} \cdot \nabla$:

$$\nabla \cdot \boldsymbol{u} = 0, \tag{1}$$

$$(\boldsymbol{u} \cdot \nabla)\, \boldsymbol{u} = -\nabla p + \mathrm{Re}^{-1} \Delta \boldsymbol{u} - h_\tau(\alpha)\, \boldsymbol{u} + \mathrm{Ri}\ \theta, \tag{2}$$

$$\nabla \cdot (\boldsymbol{u}\theta) = \mathrm{Re}^{-1}\mathrm{Pr}^{-1} \nabla \cdot (k_\tau(\alpha)\, \nabla\theta), \tag{3}$$

$$\begin{array}{llll} \boldsymbol{u} = 0, & \nabla_n p = 0, & \theta = 1 & \text{on } \Gamma_1, \\ \boldsymbol{u} = 0, & \nabla_n p = 0, & \nabla_n \theta = 0 & \text{on } \Gamma_2, \\ \boldsymbol{u} = u_i \boldsymbol{e}_x, & \nabla_n p = 0, & \theta = 0 & \text{on } \Gamma_i, \\ \nabla_n \boldsymbol{u} = 0, & p = 0, & \nabla_n \theta = 0 & \text{on } \Gamma_o. \end{array} \tag{4}$$

The flow enters the domain Ω by the inlet on boundary Γ_i and goes out by the outlet Γ_o. The domain is enclosed partially surrounded by hot walls Γ_1 and some adiabatic walls on Γ_2, as presented on Figure 2. The non-dimensional velocity $\boldsymbol{u}$ is defined by $\boldsymbol{u} = \frac{\boldsymbol{u}^\star}{U}$ where $U = 1$ is related to the inlet velocity. The non-dimensional pressure p is defined as $p = \frac{p^\star}{0.5\rho U^2}$ where ρ is the volumic mass of the fluid. The fields $\boldsymbol{u}^\star$ and $p^\star$ are the dimensioned velocity and pressure fields. The non-dimensional temperature θ is defined as $\theta = \frac{T - T_{\mathrm{ref}}}{T_{\mathrm{wall}} - T_{\mathrm{ref}}}$ where T is the dimensioned temperature field, T_{wall} is the temperature imposed on the heated boundary Γ_1 and T_{ref} is a reference temperature. Note that the non-dimensional temperature on the hot wall is thus $\theta_{\mathrm{wall}} = 1$.

In the above system, we have some non-dimensional numbers that are defined below. The Reynolds number is $\mathrm{Re} = \frac{UL}{\nu}$ where ν is the kinematic viscosity of the fluid. The Richardson number is $\mathrm{Ri} = \frac{\mathrm{Gr}_b}{\mathrm{Re}^2}$ and represents the balance between gravitational energy and the flow's kinetic energy. The modified Grashof $\mathrm{Gr}_b = \frac{g\beta\Delta T L^3}{\nu^2}$, where $\Delta T = T_{\mathrm{wall}} - T_{\mathrm{ref}}$ represents the flow balance of the magnitude of buoyancy force towards the magnitude of the viscous force. The Prandtl number $\mathrm{Pr} = \frac{\nu}{k}$ is the ratio between the momentum and thermal diffusivities.

2.1. Interpolation functions

Note that $h_\tau(\alpha)$ ideally take only binary values $h_\tau(\alpha) \in \{0, +\infty\}$ where $h_\tau(\alpha) = 0$ indicates the fluid zones and $h_\tau(\alpha) = +\infty$ the solid zones. Since such constraint can be hardly used in an optimization algorithm, the latter is relaxed first by considering $0 \leq \alpha \leq \alpha_{\max}$ for large enough $\alpha_{\max}$ and next with so-called interpolation function that are smooth regularization of step-like functions.

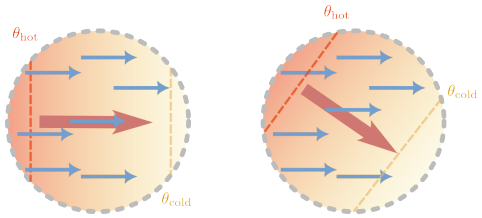

Figure 1: Orientation of heat flux field (red arrow) towards velocity field (blue arrows).The dashed lines represent iso-thermal of hot (red dashed-line) and cold temperature. (yellow dashed-line). — Left: Fields are collinear, heat is well convected. — Right: There is an angle between field, heat is less convected to the right of the domain.

Since the pseudo-inverse permeability α is a scalar field where $\alpha \in [0, \alpha_{\max}]$, using it directly to penalize the physical equations may lead to some parts of the domain Ω where the physical matter has an intermediate physical behavior between solid and fluid. This may lead to optimization results that are not physical. To overcome this issue, several penalization techniques are used in the literature. One common approach is the RAMP function [2, 7, 8],but the approach used herein is the one proposed by Ramalingom et al. [9] with some sigmoid function which shows smaller transitions area between the fluid and solid behavior than the RAMP approach. Some comparisons between the RAMP and sigmoid interpolation functions have been done in [12] and it has been shown that any choice give similar results.

The pseudo-inverse permeability can be then interpolated with the expression (5) where α_0 and τ are, respectively, the pseudo inverse permeability threshold and the slope of the sigmoid function, and $\alpha_{\max}$ is the maximum value that can be taken by the design parameter α. The thermal diffusivity is interpolated with the sigmoid function (6) where k_f and k_s are, respectively, the fluid and the solid thermal diffusivities.

$$h_\tau(\alpha) = \quad \alpha_{\max} \left(\frac{1}{1 + \mathrm{e}^{-\tau(\alpha - \alpha_0)}} - \frac{1}{1 + \mathrm{e}^{\tau\alpha_0}} \right), \tag{5}$$

$$k_\tau(\alpha) = \left(\frac{k_s}{k_f} - 1 \right) \left(\frac{1}{1 + \mathrm{e}^{-\tau(\alpha - \alpha_0)}} - \frac{1}{1 + \mathrm{e}^{\tau\alpha_0}} \right) + 1. \tag{6}$$

It is worth noting that $\lim\limits_{\alpha \to 0} h_\tau(\alpha) = 0$, $\lim\limits_{\alpha \to 0} k_\tau(\alpha) = 1$, $\lim\limits_{\alpha \to \alpha_{\max}} h_\tau(\alpha) = \alpha_{\max}$ and $\lim\limits_{\alpha \to \alpha_{\max}} k_\tau(\alpha) = \frac{k_s}{k_f}$.

3. Definition of the cosine cost function

The objective function we propose is closely related to the inner orientation within the domain of the velocity and the heat flux fields. As it is pictured on the left part of Figure 1, if the velocity field is collinear towards the heat flux, it

can be assumed that the heat is well convected towards the velocity direction. The right part of Figure 1 represents a heat flux vector field that is not collinear to the velocity field. The heat will be less effectively convected towards the direction of the velocity field than in the first case. The angle between these two vector fields is directly linked to the definition of cosine. Hence, it can be natural to define an objective function based on the cosine field between the velocity and heat flux. The idea is that obtaining a cosine of 1 (collinear vectors) leads to better heat transfer than other values. Therefore, it should be interesting to maximize the following cost function:

$$\mathcal{J}_{\cos}(\boldsymbol{u},\theta) = \int_{\mathcal{U}} \left(\frac{\boldsymbol{u}\cdot\nabla\theta}{\|\boldsymbol{u}\|\,\|\nabla\theta\|} \right) \,\mathrm{d}\Omega, \tag{7}$$

where the fraction in the integral is the cosine between the two vector fields $\boldsymbol{u}$ and $\nabla\theta$. This angle is commonly called β in the FSP framework. In its critique of the FSP, Bejan stated in [26] :
"The angle β is not a degree of freedom, a knob to be turned by the designer. There is an infinity of angles β distributed throughout the flow field, and each β depends on its neighbors (β is a field). The distribution of β is one, and it is fixed, just like the distribution of T and (u, v) in the specified flow configuration." This paper fairly tries to influence the flow field and heat exchange performances by having an objective function based actually on the β field in order to try *"to turn down the knob"*.

To go further the above considerations, it can be shown that our approach is related to the *classical* cost function that aims at maximizing thermal power

$$\mathcal{J}_2(\boldsymbol{u},\theta) = \int_{\partial\Omega} \boldsymbol{u}\cdot\boldsymbol{n}\,\theta \,\mathrm{d}\Gamma. \tag{8}$$

Such functional that involves the values of physical quantities at the inlet and outlet of the system are going to be referred as *global cost function*. *Local* cost functions are then going to be functions defined on the whole computational domain Ω. The idea behind local cost function is to use cost functions to define correlations between local flow parameters and their global impact.

Using Green's formula and the incompressibility condition, one gets

$$\mathcal{J}_2(\boldsymbol{u},\theta) = \int_{\Omega} \nabla\cdot(\boldsymbol{u}\theta) \,\mathrm{d}\Omega = \int_{\Omega} \boldsymbol{u}\cdot\nabla\theta \,\mathrm{d}\Omega.$$

From Cauchy-Schwarz inequality, we have

$$-\|\boldsymbol{u}\|\,\|\nabla\theta\| \le \boldsymbol{u}\cdot\nabla\theta \le \|\boldsymbol{u}\|\,\|\nabla\theta\|,$$

and thus the maximal values of the function $x\in\Omega \mapsto \boldsymbol{u}(x)\cdot\nabla\theta(x)$ are reached as soon as $\boldsymbol{u}\cdot\nabla\theta = \|\boldsymbol{u}\|\,\|\nabla\theta\|$. From the definition of the scalar product, this translates to

$$\cos(\angle[\boldsymbol{u},\nabla\theta]) = \frac{\boldsymbol{u}\cdot\nabla\theta}{\|\boldsymbol{u}\|\,\|\nabla\theta\|} = 1,$$

which indicates that the vector fields $x \in \Omega \mapsto \boldsymbol{u}(x)$ and $x \in \Omega \mapsto \nabla\theta(x)$ are collinear pointing in the same direction.

To highlight further the effect of the angle between $\boldsymbol{u}$ and $\nabla\theta$ on heat transfer, we now estimate the heat flow across some surface $\partial\mathcal{U}$ where $\mathcal{U}$ is a subset of Ω. We then consider two sets of velocity fields/temperatures $\boldsymbol{u}_1, \theta_1$ and $\boldsymbol{u}_2, \theta_2$ such that both velocities, respectively gradient of temperature, have same length but the angle between them is varying (see e.g. what is shown in Figure 1). Hence:

$$\begin{aligned} \forall x \in \mathcal{U}: \qquad & \|\boldsymbol{u}_1(x)\| = \|\boldsymbol{u_2}(x)\|\,, \ \|\nabla\theta_1(x)\| = \|\nabla\theta_2(x)\|\,, \\ & \cos(\angle[\boldsymbol{u}_1(x), \nabla\theta_1(x)]) < \cos(\angle[\boldsymbol{u}_2(x), \nabla\theta_2(x)]). \end{aligned}$$

Integrating the energy equation (3) over $\mathcal{U}$ and using Green's formula give

$$\int_{\partial\mathcal{U}} \mathrm{Re}^{-1}\mathrm{Pr}^{-1} k_\tau(\alpha)\nabla\theta \cdot \boldsymbol{n}_s \, d\Gamma = \int_{\mathcal{U}} \|\boldsymbol{u}\| \, \|\nabla\theta\| \cos(\angle[\boldsymbol{u}, \nabla\theta]) \, dx,$$

where $\boldsymbol{n}_s$ is the outward unitary normal to $\partial\mathcal{U}$. Introducing the heat flux density $\boldsymbol{j}(\theta) = k_\tau(\alpha)\nabla\theta \cdot \boldsymbol{n}_s$ and using the previous computation, we obtain

$$\Phi(\theta, \boldsymbol{u}) = \int_{\partial\mathcal{U}} \boldsymbol{j}(\theta) \cdot \boldsymbol{n}_s \, d\Gamma = \mathrm{Re}\,\mathrm{Pr} \int_{\mathcal{U}} \|\boldsymbol{u}\| \, \|\nabla\theta\| \cos(\angle[\boldsymbol{u}, \nabla\theta]) \, dx, \tag{9}$$

where $\Phi(\theta, \boldsymbol{u})$ is the heat flow. From (9), it follows that the heat flows associated to $(\boldsymbol{u}_1, \nabla\theta_1)$ and $(\boldsymbol{u}_2, \nabla\theta_2)$ verify

$$\Phi(\theta_1, \boldsymbol{u}_1) < \Phi(\theta_2, \boldsymbol{u}_2).$$

From this inequality, we see that for velocity and gradient of temperature with same length, the heat flow increases with the decreases of the angle between $\boldsymbol{u}$ and $\nabla\theta$, namely with the increases of the value of $\cos(\angle[\boldsymbol{u}, \nabla\theta])$ (see also [25, Eq. (4)] for a similar conclusion). Therefore, it is expected that maximizing $\cos(\angle[\boldsymbol{u}, \nabla\theta])$ will increase the heat flux which motivates using $\mathcal{J}_{\cos}$ as cost function.

Remark 1. *Similarly, if we consider velocity $\boldsymbol{u}_i$ and temperature gradients $\nabla\theta_i$ having same angle but different norms, namely satisfying*

$$\begin{aligned} \forall x \in \mathcal{U}: \qquad & \|\boldsymbol{u}_1(x)\| \, \|\nabla\theta_1(x)\| \leq \|\boldsymbol{u_2}(x)\| \, \|\nabla\theta_2(x)\|\,, \\ & 0 < \cos(\angle[\boldsymbol{u}_1(x), \nabla\theta_1(x)]) = \cos(\angle[\boldsymbol{u}_2(x), \nabla\theta_2(x)]). \end{aligned}$$

In that case, one can see from (9), we get

$$\Phi(\theta_1, \boldsymbol{u}_1) < \Phi(\theta_2, \boldsymbol{u}_2).$$

As a result, the heat flux can also be increased by increasing the norm of the velocity field and the temperature gradient. Nevertheless, as indicated in the introduction, since the field synergy angle is widely used in the literature [28, 29], we are going to use the cosine as cost function in our topology optimization problem defined in the next section (see (11)).

To end, this section, we emphasize that in the solid zones of the computational domain, the velocity is penalized so that we have $\boldsymbol{u} \approx 0$. This could yield indeterminate values (e.g. $0/0$) in the cosine cost function (7). To avoid such behavior, we will consider the following modification of the cosine cost function

$$\mathcal{J}_{\cos}(\boldsymbol{u}, \theta) = \int_{\mathcal{U}} \left(\frac{\boldsymbol{u} \cdot \nabla\theta}{\|\boldsymbol{u}\| \, \|\nabla\theta\| + s} \right) \, \mathrm{d}\Omega, \tag{10}$$

where a small scalar s fixed to 10^{-6} has been added to the denominator to regularize the function near zero. The function is then zero when the velocity or heat flux magnitudes are zero.

4. Adjoint-based solver for the topology optimization problem

We now want to minimize the following multi-objective functional :

$$\begin{aligned} \min \quad & \mathcal{J}(\boldsymbol{u}, p, \theta) = \mathrm{c}_1 \, \mathcal{J}_1(\boldsymbol{u}, p, \theta) - \mathrm{c}_2 \, \mathcal{J}_2(\boldsymbol{u}, p, \theta) - \mathrm{c}_3 \, \mathcal{J}_{\cos}(\boldsymbol{u}, p, \theta), \\ & \text{where } (\boldsymbol{u}, p, \theta) \text{ are subject to } (1, 2, 3), (4), \end{aligned} \tag{11}$$

where the first cost function $\mathcal{J}_1$ aims at minimizing pressure losses and is defined by

$$\mathcal{J}_1(\boldsymbol{u}, p) = -\int_{\partial\Omega} \boldsymbol{u} \cdot \boldsymbol{n} \left(p + \frac{1}{2} \|\boldsymbol{u}\|^2 \right) \, \mathrm{d}\Gamma. \tag{12}$$

The cost function $\mathcal{J}_2$ is defined by (8) and will be maximised. We emphasize that $\mathcal{J}_2$ is a classical objective function used in the literature, aiming to improve the thermal power gain through the domain. The constants c_1, c_2 and c_3 are the so-called weigh factors of the objective functions in the framework of multi-objective optimization. Since $\mathcal{J}_2$ and $\mathcal{J}_{\cos}$ objective functions are meant to be maximized, it is equivalent to minimize their opposite. This explains the minus sign facing these objective functions in (11).

We solve the topology optimization problem (11) with a gradient-descent algorithm. The gradient of the cost function with respect to the design variable α is computed with the continuous adjoint method (see e.g. [35]). The adjoint system is defined as the critical point of the following Lagrangian with respect to the so-called primal variables $(\boldsymbol{u}, p, \theta)$

$$\begin{aligned} \mathcal{L}(\boldsymbol{u}, \theta, p, \boldsymbol{u^*}, \theta^*, p^*, \alpha) = \quad & \mathcal{J}(\boldsymbol{u}, \theta, p) \\ & + \int_\Omega p^* \nabla \cdot \boldsymbol{u} \, \mathrm{d}\Omega \\ & + \int_\Omega \boldsymbol{u^*} \left[(\boldsymbol{u} \cdot \nabla) \, \boldsymbol{u} + \nabla p - A\Delta\boldsymbol{u} + h_\tau(\alpha)\boldsymbol{u} - B\theta\boldsymbol{e_y} \right] d\Omega \\ & + \int_\Omega \theta^* \left[\nabla \cdot (\boldsymbol{u}\theta) - \nabla \cdot (Ck_\tau(\alpha)\nabla\theta) \right] \, \mathrm{d}\Omega, \end{aligned} \tag{13}$$

where $(\boldsymbol{u}^*, p^*, \theta^*)$ are the adjoint variables. In the sequel, we first compute the derivative of $\mathcal{J}$ with respect to $(\boldsymbol{u}, p, \theta)$ and give next the adjoint problem. We end this section with the algorithm used to solve the topology optimization problem (11) involving the local cost function.

4.1. Derivatives of the cost functions

For any function $F : \mathbf{X} \to \mathbb{R}$ where $\mathbf{X}$ is a normed space, the Gateaux (directional) derivative is defined as

$$\frac{\partial F}{\partial x}[\delta x] = \lim_{t \to 0} \frac{F(x + t\,\delta x) - F(x)}{t}.$$

Assuming also that $\mathbf{X}$ is a Hilbert space equipped with an inner product $(\cdot, \cdot)_{\mathbf{X}}$, we can define the gradient of F, denoted here by $\frac{\partial F}{\partial x}$ thanks to the identification

$$\frac{\partial F}{\partial x}[\delta x] = \left(\frac{\partial F}{\partial x}, \delta x \right)_{\mathbf{X}}.$$

Below, we will identify gradients of the functionals using the L^2-inner product

$$(\boldsymbol{u}, \boldsymbol{v}) := \int_\Omega \boldsymbol{u} \cdot \boldsymbol{v} \ \mathrm{d}\Omega,$$

which is defined accordingly for scalar valued functions.

For the cost function considered in this paper, we have

$$\begin{aligned} \frac{\partial \mathcal{J}}{\partial(\boldsymbol{u}, p, \theta)}[\delta\boldsymbol{u}, \delta p, \delta\theta] &= c_1 \frac{\partial \mathcal{J}_1}{\partial(\boldsymbol{u}, p, \theta)}[\delta\boldsymbol{u}, \delta p, \delta\theta] - c_2 \frac{\partial \mathcal{J}_2}{\partial(\boldsymbol{u}, p, \theta)}[\delta\boldsymbol{u}, \delta p, \delta\theta] \\ &- c_3 \frac{\partial \mathcal{J}_{\cos}}{\partial(\boldsymbol{u}, p, \theta)}[\delta\boldsymbol{u}, \delta p, \delta\theta], \end{aligned}$$

and we now compute each term. For the pressure losses functional, we have

$$\frac{\partial \mathcal{J}_1}{\partial(\boldsymbol{u}, p, \theta)}[\delta\boldsymbol{u}, \delta p, \delta\theta] = -\int_\Gamma \boldsymbol{u} \cdot \boldsymbol{n} \ \delta p \ \mathrm{d}\Gamma - \int_\Gamma (p_t \boldsymbol{n} + (\boldsymbol{u} \cdot \boldsymbol{n})\, \boldsymbol{u}) \cdot \delta\boldsymbol{u} \ \mathrm{d}\Gamma,$$

where $p_t = p + \|\boldsymbol{u}\|^2 / 2$ is the total pressure. For the thermal power cost function, one has

$$\frac{\partial \mathcal{J}_2}{\partial(\boldsymbol{u}, p, \theta)}[\delta\boldsymbol{u}, \delta p, \delta\theta] = \int_\Gamma \boldsymbol{u} \cdot \boldsymbol{n} \ \delta\theta \ \mathrm{d}\Gamma + \int_\Gamma \theta \ \boldsymbol{n} \cdot \delta\boldsymbol{u} \ \mathrm{d}\Gamma.$$

Before computing the derivative of the proposed local cost function, we recall that the derivative of the Euclidean norm $N : x \in \mathbb{R}^N \mapsto \|x\| \in \mathbb{R}$ is

$$\frac{\partial N}{\partial x}[\delta x] = \frac{x}{\|x\|} \cdot \delta x.$$

Using this, the derivative of the local (cosine) cost function is

$$
\begin{aligned}
&\frac{\partial \mathcal{J}_{\cos}}{\partial(\boldsymbol{u},p,\theta)}[\delta\boldsymbol{u},\delta p,\delta\theta] = \frac{\partial \mathcal{J}_{\cos}}{\partial \boldsymbol{u}}[\delta\boldsymbol{u}] + \frac{\partial \mathcal{J}_{\cos}}{\partial \theta}[\delta\theta] \\
= &\int_\Omega \delta\boldsymbol{u}\cdot\frac{1}{\left(\|\boldsymbol{u}\|\,\|\nabla\theta\|+s\right)^2}\left[\nabla\theta\left(\|\boldsymbol{u}\|\,\|\nabla\theta\|+s\right)-\left(\boldsymbol{u}\cdot\nabla\theta\right)\frac{\boldsymbol{u}}{\|u\|}\,\|\nabla\theta\|\right]\,\mathrm{d}\Omega \\
+ &\int_\Omega \nabla\delta\theta\cdot\frac{1}{\left(\|\boldsymbol{u}\|\,\|\nabla\theta\|+s\right)^2}\left[\boldsymbol{u}\left(\|\boldsymbol{u}\|\,\|\nabla\theta\|+s\right)-\left(\boldsymbol{u}\cdot\nabla\theta\right)\frac{\nabla\theta}{\|\nabla\theta\|}\,\|\boldsymbol{u}\|\right]\,\mathrm{d}\Omega \\
= &\int_\Omega \delta\boldsymbol{u}\cdot\left(\boldsymbol{\psi}(\boldsymbol{u},\theta)\right)\,\mathrm{d}\Omega + \int_\Gamma \delta\theta\,\boldsymbol{\phi}(\boldsymbol{u},\theta)\cdot\boldsymbol{n}\,\mathrm{d}\Gamma - \int_\Omega \delta\theta\,\nabla\cdot\left(\boldsymbol{\phi}(\boldsymbol{u},\theta)\right)\,\mathrm{d}\Omega,
\end{aligned}
$$

where

$$
\begin{aligned}
\boldsymbol{\psi}(\boldsymbol{u},\theta) &= \frac{1}{\left(\|\boldsymbol{u}\|\,\|\nabla\theta\|+s\right)^2}\left[\nabla\theta\left(\|\boldsymbol{u}\|\,\|\nabla\theta\|+s\right)-\left(\boldsymbol{u}\cdot\nabla\theta\right)\frac{\boldsymbol{u}}{\|u\|}\,\|\nabla\theta\|\right], \\
\boldsymbol{\phi}(\boldsymbol{u},\theta) &= \frac{1}{\left(\|\boldsymbol{u}\|\,\|\nabla\theta\|+s\right)^2}\left[\boldsymbol{u}\left(\|\boldsymbol{u}\|\,\|\nabla\theta\|+s\right)-\left(\boldsymbol{u}\cdot\nabla\theta\right)\frac{\nabla\theta}{\|\nabla\theta\|}\,\|\boldsymbol{u}\|\right].
\end{aligned}
$$

Using the previous computations, the derivatives of the cost function $\mathcal{J}$ can be written as

$$
\frac{\partial \mathcal{J}}{\partial(\boldsymbol{u},p,\theta)}[\delta\boldsymbol{u},\delta p,\delta\theta] = \int_\Omega \frac{\partial \mathcal{J}_\Omega}{\partial(\boldsymbol{u},p,\theta)}[\delta\boldsymbol{u},\delta p,\delta\theta]\,\mathrm{d}\Omega + \int_\Gamma \frac{\partial \mathcal{J}_\Gamma}{\partial(\boldsymbol{u},p,\theta)}[\delta\boldsymbol{u},\delta p,\delta\theta]\,\mathrm{d}\Gamma,
$$

with

$$
\begin{aligned}
\frac{\partial \mathcal{J}_\Gamma}{\partial \boldsymbol{u}}[\delta\boldsymbol{u}] &= c_3\int_\Omega \delta\boldsymbol{u}\cdot\boldsymbol{\psi}(\boldsymbol{u},\theta)\,\mathrm{d}\Omega, \\
\frac{\partial \mathcal{J}_\Gamma}{\partial \theta}[\delta\theta] &= -c_3\int_\Omega \delta\theta\,\nabla\cdot\left(\boldsymbol{\phi}(\boldsymbol{u},\theta)\right)\,\mathrm{d}\Omega, \\
\frac{\partial \mathcal{J}_\Gamma}{\partial p}[\delta p] &= 0,
\end{aligned}
$$

and:

$$
\begin{aligned}
\frac{\partial \mathcal{J}_\Omega}{\partial \boldsymbol{u}}[\delta\boldsymbol{u}] &= -c_1\int_\Gamma \left(p_t\boldsymbol{n}+\left(\boldsymbol{u}\cdot\boldsymbol{n}\right)\boldsymbol{u}\right)\cdot\delta\boldsymbol{u}\,\mathrm{d}\Gamma + c_2\int_\Gamma \theta\,\boldsymbol{n}\cdot\delta\boldsymbol{u}\,\mathrm{d}\Gamma, \\
\frac{\partial \mathcal{J}_\Omega}{\partial \theta}[\delta\theta] &= +c_2\int_\Gamma \boldsymbol{u}\cdot\boldsymbol{n}\,\delta\theta\,\mathrm{d}\Gamma + c_3\int_\Gamma \boldsymbol{\phi}(\boldsymbol{u},\theta)\cdot\boldsymbol{n}\,\delta\theta\,\mathrm{d}\Gamma, \\
\frac{\partial \mathcal{J}_\Omega}{\partial p}[\delta p] &= -c_1\int_\Gamma \boldsymbol{u}\cdot\boldsymbol{n}\,\delta p\,\mathrm{d}\Gamma.
\end{aligned}
$$

4.2. Adjoint equations

The continuous adjoint system is defined as the critical points of the Lagrangian, defined in (13), with respect to the primal variables $(\boldsymbol{u},\theta,p)$. The

latter has already been computed for instance in [9] and reads as

$$\begin{aligned}
\nabla \cdot \boldsymbol{u}^* &= \frac{\partial \mathcal{J}_\Omega}{\partial p}, \\
\mathrm{Re}^{-1}\Delta \boldsymbol{u}^* + (\boldsymbol{u}\cdot\nabla)\,\boldsymbol{u}^* + (\nabla \boldsymbol{u}^*)^T \cdot \boldsymbol{u} + \nabla p^* + \theta \nabla \theta^* - h_\tau(\alpha)\boldsymbol{u}^* &= \frac{\partial \mathcal{J}_\Omega}{\partial \boldsymbol{u}}, \\
\boldsymbol{u}\cdot\nabla\theta^* + \mathrm{Re}^{-1}\mathrm{Pr}^{-1}\nabla\cdot(k\,(\alpha)\,\nabla\theta^*) &= \frac{\partial \mathcal{J}_\Omega}{\partial \theta},
\end{aligned} \tag{14}$$

supplemented with the following boundary conditions on Γ_1 and Γ_i:

$$\text{on } \Gamma_1 \cup \Gamma_i: \quad -\boldsymbol{u}^*\cdot\boldsymbol{n} = \tfrac{\partial \mathcal{J}}{\partial p},\ -\mathrm{Re}^{-1}\boldsymbol{u}^*\cdot\boldsymbol{t} = \tfrac{\partial \mathcal{J}}{\partial \boldsymbol{u}}\cdot\boldsymbol{t},\ \mathrm{Ri}\,k_\tau(\alpha)\theta^* = \tfrac{\partial \mathcal{J}}{\partial \theta}$$

$$\begin{aligned}
\text{on } \Gamma_2: \qquad -\boldsymbol{u}^*\cdot\boldsymbol{n} &= \tfrac{\partial \mathcal{J}}{\partial p},\ -\mathrm{Re}^{-1}\boldsymbol{u}^*\cdot\boldsymbol{t} = \tfrac{\partial \mathcal{J}}{\partial \boldsymbol{u}}\cdot\boldsymbol{t}, \\
-\mathrm{Ri}k_\tau(\alpha)\nabla_n\theta^* - (\boldsymbol{u}\cdot\boldsymbol{n})\theta^* &= \tfrac{\partial \mathcal{J}}{\partial \theta},
\end{aligned} \tag{15}$$

$$\begin{aligned}
\text{on } \Gamma_o: \qquad -\mathrm{Re}^{-1}\nabla_n\boldsymbol{u}^* - (\boldsymbol{u}\cdot\boldsymbol{n})\boldsymbol{u}^* - \boldsymbol{n}p^* - \boldsymbol{n}\theta\theta^* &= \tfrac{\partial \mathcal{J}}{\partial \boldsymbol{u}}, \\
-\mathrm{Ri}k_\tau(\alpha)\nabla_n\theta^* - (\boldsymbol{u}\cdot\boldsymbol{n})\theta^* &= \tfrac{\partial \mathcal{J}}{\partial \theta}.
\end{aligned}$$

The full adjoint system is therefore given by (14),(15).

4.3. Algorithm to update conception variable

Given some design variable α_k, the sensibility $\nabla\mathcal{J}_k := \dfrac{\partial \mathcal{J}}{\partial \alpha}(\alpha_k)$ is defined with the following equation:

$$\nabla\mathcal{J}_k = \frac{\partial \mathcal{J}}{\partial \alpha}(\alpha) = -\frac{\partial h_\tau}{\partial \alpha}\,\mathbf{u}\cdot\mathbf{u}^* - \mathrm{Ri}\frac{\partial k_\tau}{\partial \alpha}\nabla\theta\cdot\nabla\theta^* \quad \text{on } \Omega. \tag{16}$$

Once the adjoint set of equation is solved and the sensibility is computed, the design field α_k is then updated across the k-th update step with the gradient method using

$$\boldsymbol{\alpha}_{k+1} = \boldsymbol{\alpha}_k + \lambda_k \boldsymbol{d_k}, \tag{17}$$

where $\boldsymbol{d_k}$ is the descent direction and λ_k the step which will be constant. The design variables are evaluated by using the conjugated-gradient descent direction method associated to Polack-Ribiere method. The descent direction $\boldsymbol{d_{k+1}}$ is given by :

$$\boldsymbol{d}_{k+1} = \nabla\mathcal{J}_{k+1} + \beta_{k+1}\boldsymbol{d_k}$$

where :

$$\beta^{PR}_{k+1} = \frac{\nabla\mathcal{J}^T_{k+1}\,(\nabla\mathcal{J}_{k+1} - \nabla\mathcal{J}_k)}{\nabla\mathcal{J}^T_k\ \nabla\mathcal{J}_k}.$$

The implementation follows the Algorithm 1. The systems of equations have been solved with the finite volume library OpenFoam [36]. The algorithm follows the SIMPLE algorithm philosophy. The primal equations (1) to (4) and adjoint equations (14),(15) are solved, the sensitivity is computed with equation (16) and the design field α is updated with equation (17). The generalized

Algorithm 1 Optimization algorithm

initialization of constant Re, Ri, Pr, α_0, τ_0, s
evaluation of cost function $\mathcal{J}_0$
while $\epsilon \geq 0.01$ over 1000 iterations **do**
    solve primal equation (2) to (4) with a SIMPLE algorithm loop.
    solve adjoint equations (14), (15) with a SIMPLE algorithm loop.
    update sensitivity according to (16)
    update design field α with (17), along with $h_\tau(\alpha)$, $k_\tau(\alpha)$
    evaluation of $\mathcal{J}_k$; $\epsilon \leftarrow \dfrac{\mathcal{J}_k}{\mathcal{J}_{k-1}}$
    $\mathcal{J}_{k-1} \leftarrow \mathcal{J}_k$
    $k \leftarrow k + 1$
end while

Geometric-Algebraic Multi-Grid (GAMG) solver with a cell-centered colocalized finite volume approach is used. First order numerical schemes are used to discretize the convective terms. The optimization process is stopped when the evaluation of function remains stable at 1% over 1000 iterations of the optimization process. The current algorithm has been used in [9, 12] and will be used to get all our numerical results.

5. Numerical results

In this section, we present first the result of the CFD analysis without optimization on two geometries (single pipe and bend pipe). After that, the optimized results considering the classical multi-optimization approach $(\mathcal{J}_1, \mathcal{J}_2)$, denominated by SP1 for the single pipe and BP1 for the bend pipe, will be quantitatively and qualitatively compared to the approach proposed by this paper, namely using cost functions $(\mathcal{J}_1, \mathcal{J}_{\cos})$ in a multi-objective optimization framework for the single pipe and the bend pipe (denominated SP2 and BP2). It will be demonstrated that the results are very similar. The FSP principle will be finally confronted with the thermal power gain.

Figure 2 represents the studied geometries, their design domain Ω and their boundaries for the single pipe and the bend pipe. These configurations are some common shapes studied in the literature [9, 8, 37] to develop some new approaches to topology optimization. Both geometries are squares of side L, regularly meshed with 40,000 cuboid cells. The single pipe is a straightforward symmetrical geometry with hot walls on the top and lower walls. The inlet is located on the middle of the left wall, and the outlet on the middle of the right wall. The bend pipe has its inlet on the upper part of the left wall and its outlet on the left of the bottom wall, forcing the flow to curve its trajectory through the domain. The hot wall is on the left part of the lower wall. The inlet and outlet sizes for both geometries are $\frac{L}{5}$. The hot walls have a fixed temperature, and the other walls are adiabatic. For the two representative cases studied in

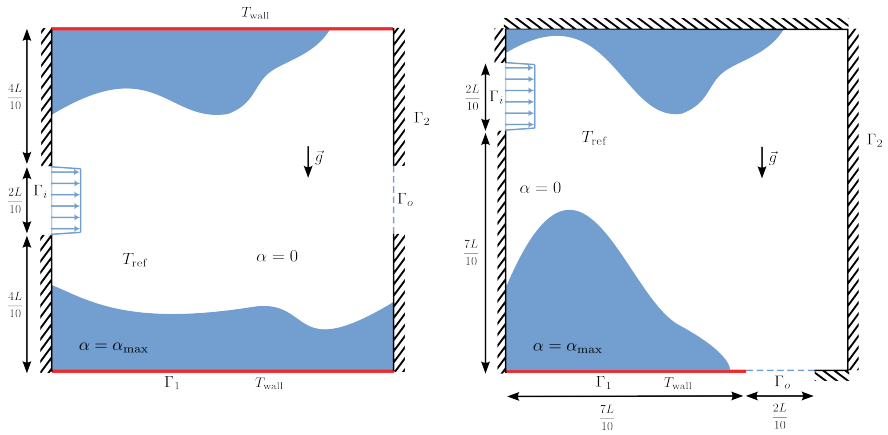

Figure 2: Right: Single pipe geometry. Left: Bend pipe geometry.

this section, the thermal diffusivity ratio used in the energy equation (3) with (6) is fixed to

$$\frac{k_s}{k_f} = 4.4,$$

representing, for example, aluminum for the solid and air for the fluid. For the sigmoid interpolation factor in (5) and (6), we set

$$\alpha_0 = 20,\ \tau = 0.7 \text{ and } \alpha_{\text{max}} = 200.$$

Prandtl number is set to $\text{Pr} = 0.71$. The Reynolds and Richardson numbers that are investigated in this paper are

$$\text{Re} = 100,\ 200,\ 400,\ \text{Ri} = 0,\ 0.3,\ 3.$$

Finally, the inlet non-dimensional velocity is set to $u_i \boldsymbol{e}_x$ with $u_i = 1$.

5.1. Results for the single pipe without optimization

Figure 3 shows the $\|u\|$, θ, $\|\nabla\theta\|$ and $\cos(\angle[\boldsymbol{u}, \nabla\theta])$ fields without optimization for the single pipe with Re=200 and Ri=0.3. The flow is straightforwardly directed from left to right, with some slight recirculation areas appearing outside the central part of the flow. The temperature field from the hot walls is diffused through the domain and is then convected by the flow through the outlet. The heat flux is pronounced near the interfaces of the main flow path. The Figure 3-(d) illustrates the cosine field, which is the integrant of the objective function $\mathcal{J}_{\cos}$ we experiment with in this article. Maximizing $\mathcal{J}_{\cos}$ will increase the average value of this field to a value closer to one. With the exception of the area of the outlet, it displays that the main flow shows positive cosine values (shade of red color on the figure) and is outlined by a negative cosine field (blue color). Areas with a zero cosine are in white. We clearly see a horizontal line

with $\cos(\angle[\boldsymbol{u}, \nabla\theta]) \approx 1$ which reveals a huge synergy. According to the FSP principle, this huge synergy should lead to a local high contribution of the flow to heat transfer. However, it can be seen on the Figure 3-(c) that the magnitude of the heat flux on this line is near zero. This observation is clearly the critic of Bejan in [26].

It is worth mentioning that the fields are not strictly symmetric because of the Richardson number and gravity, which apply a force over the vertical direction.

5.2. Results for the bend pipe without optimization

Figure 4 presents the fields for the bend pipe with Re=200 and Ri=0. The Figure 4-(d) shows the cosine field. As for the single pipe, the main part of the flow leads to a positive cosine. On the lower left part of the domain where a recirculating flow appears, the cosine alternatively takes positive and negative values. The upper part of the flow contour shows an area with $\cos(\angle[\boldsymbol{u}, \nabla\theta]) \approx 1$ while the heat flux shown on 4-(c) has minimal values near this area. This reveals some limitations of the FSP in areas distant from where local heat exchanges are low, as stated previously for the single pipe.

5.3. Comparison of Local VS global approaches: Selected cases

The shapes and flow obtained with optimization using local approaches are qualitatively comparable with the ones in [37, 9] and bring new designs of topology optimization for the single and bend pipe cases. Among all the investigated configurations tested for each set of Reynolds and Richardson numbers, and geometries, the representative cases for $\mathrm{Re} = 200$ and $\mathrm{Ri} = 0.3$, denoted as SP1, SP2, BP1 and BP2 whose parameters are shown in Table 1 will be presented. These couples have been chosen to have nearly the same performance as it will be outlined.

First of all, one can see that our algorithm succeeds in minimizing/maximizing one or other cost functions for each investigated geometry. Table 1 gives $\mathcal{J}$ values before and after optimization. We observe that the objective function decreases up to a factor 6.0 in the bend pipe, for example, and up to a factor 7.6 in the single pipe. So, our algorithm converges to an optimized solution for these studied cases. The Figure 5 presents the fields resulting from the multi-objective optimization of $(\mathcal{J}_1, \mathcal{J}_2)$ for the single pipe case SP1 in a configuration where the heat exchange is favored over the mechanical power. The optimized shape leads the flow to be split through the upper and lower part of the domain near the heating wall to gain heat and convect it through the outlet. This example outlines that our optimization process is doing its purpose since the more the fluid travels near the hot wall, the more it will gain heat and transfer it through the domain.

Figure 6 displays the optimized single pipe for the case SP2. The $h_\tau(\alpha)$ shows roughly the same shape as the case SP1 shown on Figure 5 except that some solid is put in a part of the outlet. The solid in the middle of the domain also shows some fluid within the solid, meaning that fluid is trapped inside

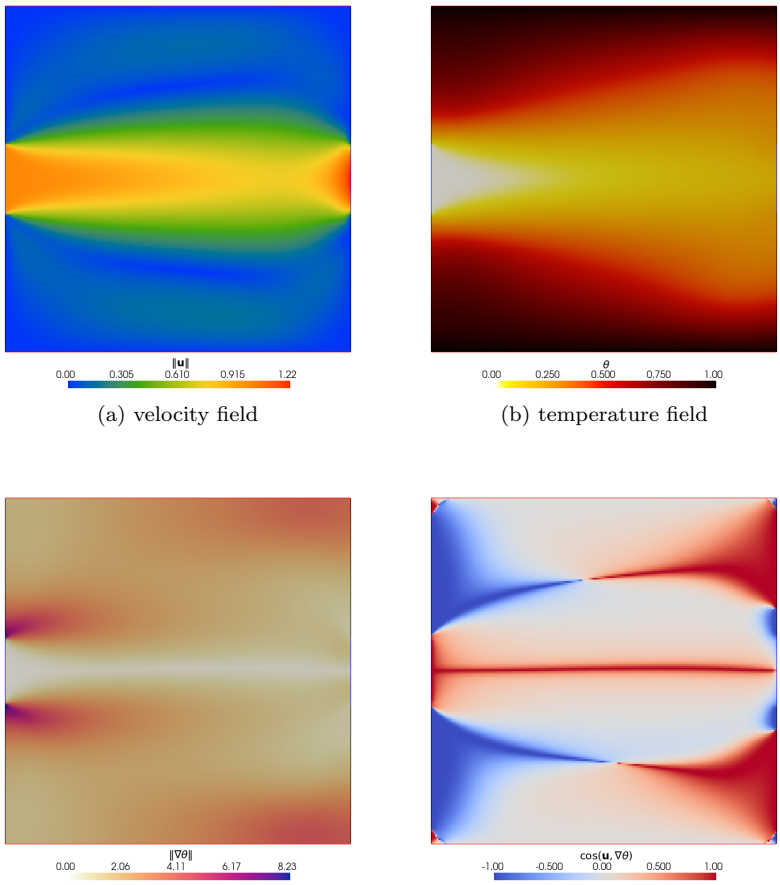

(a) velocity field

(b) temperature field

(c) heat flux field

(d) cosine field

Figure 3: Field of the single pipe – no optimization – Re = 200 and Ri = 0.3

Name	Geometry	c_1	c_2	c_3	$\mathcal{J}_0$	$\mathcal{J}_{\text{opt}}$	R_{opt}
SP1	Single pipe	0.016	0.984	0.	-0.0063	-0.0224	3.5
SP2	Single pipe	1.	0	1.9	-0.0078	-0.0591	7.6
BP1	Bend pipe	0.01	0.99	0.	-0.0024	-0.0062	2.6
BP2	Bend pipe	1.	0	9.6	-0.0895	-0.5380	6.0

Table 1: Abbreviation used for several cases in the present paper, for Re = 200 and Ri=0.3. $\mathcal{J}_0$ is the cost function evaluated without optimization. $\mathcal{J}_{\text{opt}}$ is the value of the cost function with optimization. R_{opt} is the ratio of improvement of the objective function.

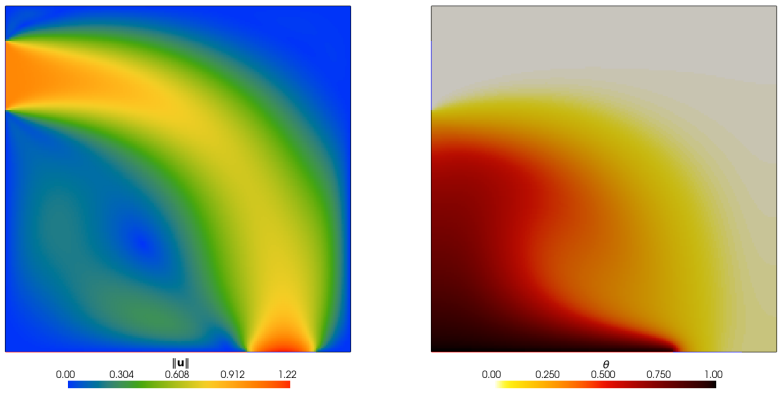

(a) velocity field

(b) temperature field

(c) heat flux field

(d) cosine field

Figure 4: Field of the bend pipe – no optimization – Re = 200 and Ri = 0.3

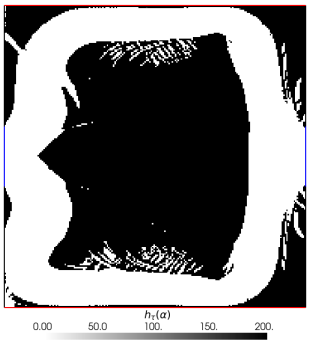

(a) $h_\tau(\alpha)$

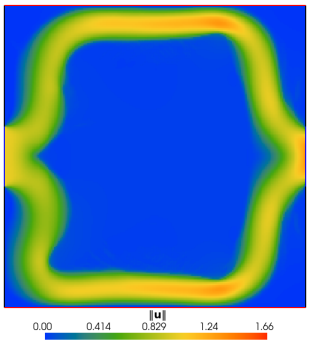

(b) $\|\boldsymbol{u}\|$

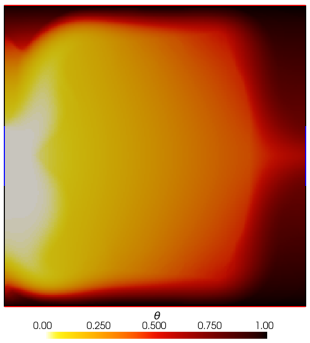

(c) θ

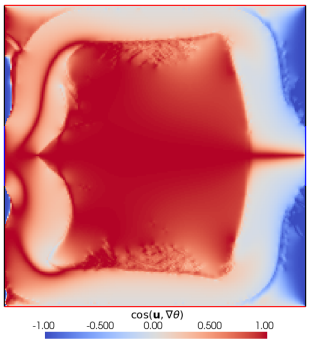

(d) $\cos(\angle[\boldsymbol{u}, \nabla\theta])$

Figure 5: Fields for the single pipe case SP1 – Optimization of $(\mathcal{J}_1, \mathcal{J}_2)$

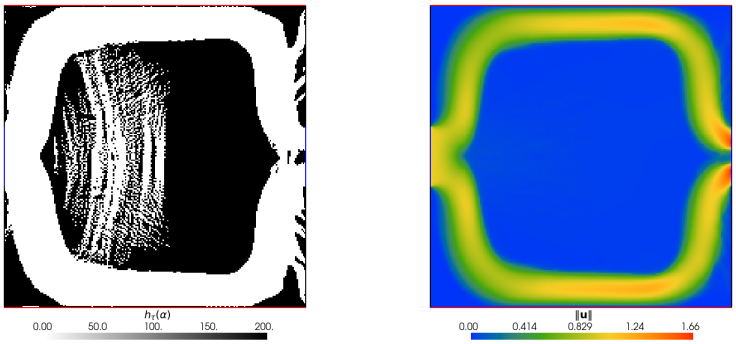

(a) $h_\tau(\alpha)$ (b) $\|\boldsymbol{u}\|$

(c) θ (d) $\cos(\angle[\boldsymbol{u}, \nabla\theta])$

Figure 6: Fields for the single pipe case SP2 – Optimization of $(\mathcal{J}_1, \mathcal{J}_{\cos})$

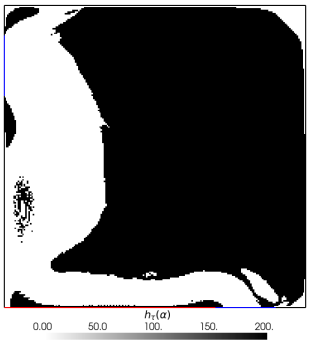

(a) $h_\tau(\alpha)$

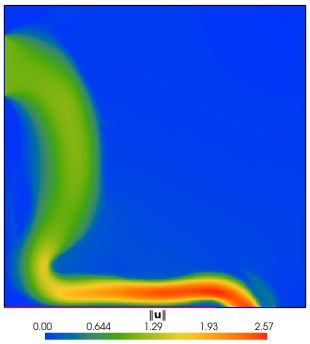

(b) $\|\boldsymbol{u}\|$

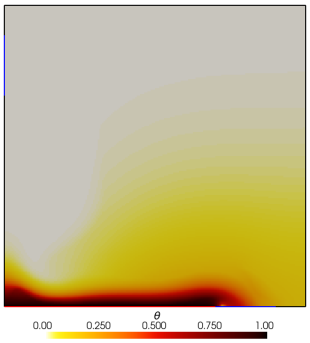

(c) θ

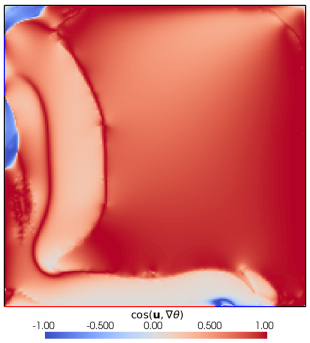

(d) $\cos(\angle[\boldsymbol{u}, \nabla\theta])$

Figure 7: Fields for the bend pipe BP1 – Optimization of $(\mathcal{J}_1, \mathcal{J}_2)$

(a) $h_\tau(\alpha)$

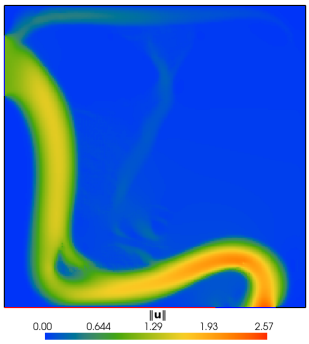

(b) $\|\boldsymbol{u}\|$

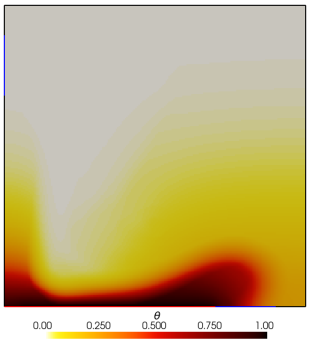

(c) θ

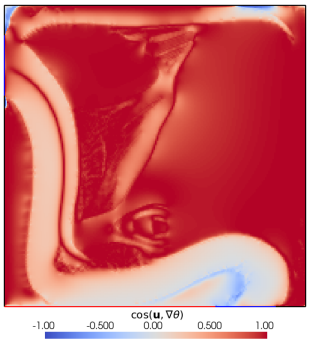

(d) $\cos(\angle[\boldsymbol{u}, \nabla\theta])$

Figure 8: Fields for the bend pipe BP2 – Optimization of $(\mathcal{J}_1, \mathcal{J}_{\cos})$

the solid region. This phenomenon is a known drawback of the density-based topology optimization approaches and may appear with multi-physics problems [3].

For the single pipe cases SP1 and SP2, even if the shape differs a little, the plot of the magnitude of the velocity shows that in both cases, the flow is split in two by a solid internal shape, with comparable velocity amplitude. One part of the flux is directed toward the heating wall to gain heat, while the other goes more straightforwardly to the outlet. We can see on the $h_\tau(\alpha)$ field for $(\mathcal{J}_1, \mathcal{J}_{\cos})$ (case SP2) that even if the solid part is less closed than the one with the classical approach (case SP1), the flow is well canalized as it can be seen on the magnitude of the velocity figures. Looking at the $\cos(\angle[\boldsymbol{u}, \nabla\theta])$ field, we can see that the case SP2 shows less negative cosine (blue area) than the SP1 case. This was attended since, in the SP2 case, the objective function involves the maximization of $\mathcal{J}_{\cos}$, which tend to increase the mean values of the $\cos(\angle[\boldsymbol{u}, \nabla\theta])$ field. It can be concluded that even if the density field $h_\tau(\alpha)$ may look different, nearly the same velocity and temperature fields are obtained for both cases. This correspondence qualitatively confirms that the cosine objective function $\mathcal{J}_{\cos}$ is closed to the classical $\mathcal{J}_2$ objective function in this case.

Figures 7 and 8 display the optimized bend pipe cases, BP1 and BP2. For both cases, the optimized shape presents a huge solid in most of the middle to right part of the domain. This shape makes the flow be pushed through the hot wall in order to gain heat that will be convected to the outlet, leading to increased heat exchanges. For BP2 the temperature field $h_\tau(\alpha)$ shows a shape of bulbs near the outlet. This make the temperature field spread a little more away from the hot wall. The amplitude of velocity and the velocity field are comparable even if a "leak" occurs inside the upper middle part of the solid BP2 shape. For the BP2 case with the optimization of $(\mathcal{J}_1, \mathcal{J}_{\cos})$, as for the case SP2, the solid area is less continuously defined as it is the case for the use of $(\mathcal{J}_1, \mathcal{J}_2)$. As for the single pipe SP1 and SP2, and for the same reason, the cosine field for BP2 shows nearly only positive values (in red on the figure) when more negative values are present for BP1. Nevertheless, from a qualitative point of view, both cases BP1 and BP2 are considered very similar.

The thermal power gain in each couple of cases is comparable from a quantitative point of view. Table 2 shows the values obtained for each case. Comparing SP1 and SP2, the mechanical power loss is lower by 0.5% for SP2, and the thermal power gain is nearly the same, close to 0.06%. Between BP1 and BP2, the mechanical power loss is lower by 5.% for BP2, and the thermal power gain is nearly the same, close to 0.006%. Meaning that BP2 shows better mechanical performance for the same heat exchanged. Note that these points have been voluntarily chosen to be close in performance. A panorama of all the tested configurations will be presented in the following subsection.

5.4. Local VS global approaches: Pareto fronts

Since we wish to study the effect of the optimization of the local cost function on the heat transfer, we are going to consider the following multi-objective cases

Case	Mechanical power loss	Thermal power gain
SP1	0.1592	0.02537
SP2	0.1584	0.02549
BP1	0.1724	0.00795
BP2	0.1649	0.00796

Table 2: Numerical values obtained after for different optimized cases

in the frame of optimization problem (11):

$$c_1 \in [0,1],\ c_2 \in [0,1],\ c_3 = 0 \text{ for } \mathcal{J} = c_1\mathcal{J}_1 - c_2\mathcal{J}_2 \text{ (classical approach)}$$
$$c_1 = 1,\ c_2 = 0,\ c_3 \in [0,50] \text{ for } \mathcal{J} = c_1\mathcal{J}_1 - c_3\mathcal{J}_{\cos} \text{ (local approach)}$$

Several weight factors c_1, c_2 and c_3 for each objective have been chosen in order to sweep the space between favoring the flow (12) or enhancing thermal exchange ((8) or (10)). This will allow next to present each performance on a Pareto front where it has been chosen to plot the performance of each numerical experiment regarding thermal power gain and mechanical power loss.

In order to represents the whole set of weights factor of each couple of Reynolds and Richardson, Pareto front showing the performance of each case has been computed. The Pareto front including the cases SP1 and SP2 for the single pipe is shown on Figure 9 while the one including BP1 and BP2 is shown on Figure 10 for the bend pipe. The couple SP1, SP2 and BP1, BP2 are each time presented with cross marker instead of circle markers. As stated above, they are nearly superposed because they were chosen to give the same performance. The abscissa is the mechanical power loss between the inlet and the outlet. This power loss corresponds to the objective function $\mathcal{J}_1$ defined in (12). The ordinate represents the thermal power gain between the inlet and outlet, corresponding to the objective function $\mathcal{J}_2$ defined in (8). For each Pareto front, the unreachable point corresponding to the best performance of thermal power gain and power loss of the considering set of results of all cases for a geometry, Reynolds and Richardson are shown as the "Utopia" point. Proposition : The "Utopia" point is defined for each Pareto front as the unreachable point corresponding to the best performance of thermal power gain and power loss, among obtained results for a given geometry, Reynolds numbers and Richardson numbers. The blue, yellow and gray point represent the performance of the objective function $\mathcal{J}_1$, $\mathcal{J}_2$ and $\mathcal{J}_{\cos}$ optimized alone. The purple point presents the performance without optimization. The green points represent the performance for each tested couple of (c_1, c_3) for $(\mathcal{J}_1, \mathcal{J}_{\cos})$ while the red points represent the performance for each tested couple of (c_1, c_2) for $(\mathcal{J}_1, \mathcal{J}_2)$. The points indicating the most important performance are linked by a blue dashed line representing the Pareto front.

For the single pipe, Figure 9 highlights that in the tested range of weighting factor, the $(\mathcal{J}_1, \mathcal{J}_2)$ and $(\mathcal{J}_1, \mathcal{J}_{\cos})$ points are mostly superposed with sometimes $(\mathcal{J}_1, \mathcal{J}_{\cos})$ dominating the Pareto front when sometimes $(\mathcal{J}_1, \mathcal{J}_2)$ dominating

the Pareto front. It should be noted that when approaching the mechanical power loss of $\mathcal{J}_2$ alone (yellow point), the limits of the current methodology is reached since the domain are mostly all filled with solid and the solids show many leaks with no clear path of the flow from the inlet to the outlet. Although, the objective functions are still minimized. For the bend pipe, the Pareto front Figure 9 shows that most of the time, the $(\mathcal{J}_1, \mathcal{J}_2)$ points dominate the other point except in an area where mechanical power loss ranges from 0.1 to 0.2 where $(\mathcal{J}_1, \mathcal{J}_{\cos})$ lead to better performance.

This comforts the previous assertion that the $\mathcal{J}_{\cos}$ objective function leads to optimized results which may be comparable to those obtained with the classic approach, meaning that a designer could consider this multi-objective optimization of thermal power gain and mechanical power reduction by also taking into account the fields synergy principle.

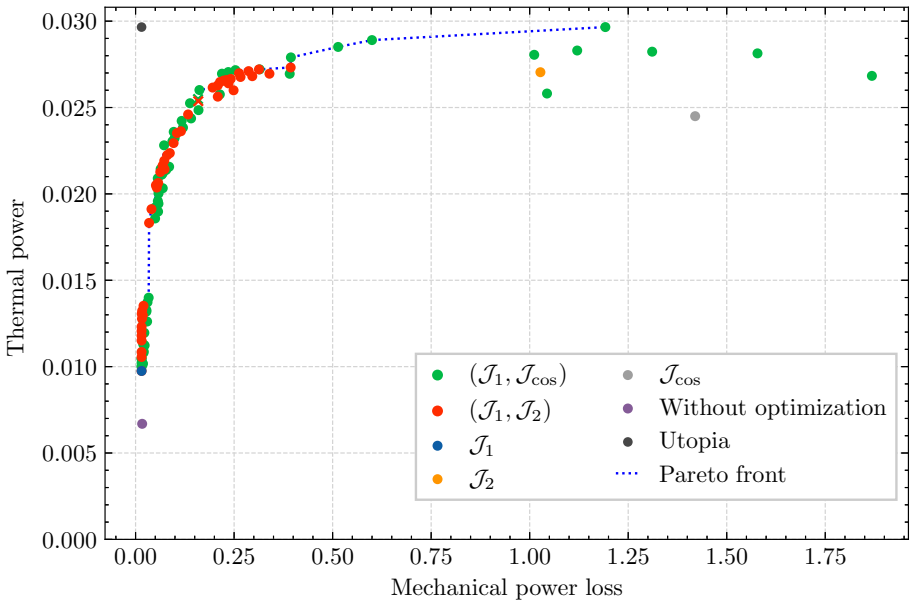

Figure 9: Pareto front for the single pipe – Re = 200 and Ri = 0.3

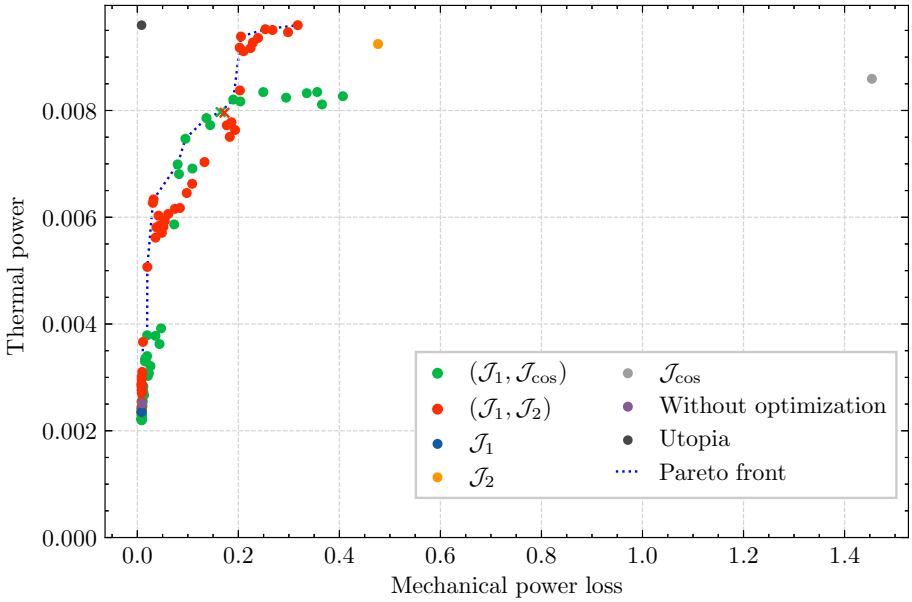

Figure 10: Pareto front for the bend pipe – Re = 200 and Ri = 0.3

5.5. Thermal power gain VS field synergy angle

The field synergy principle will be now confronted to the thermal power gain. To achieve this, we rely on the mean field synergy angle which is defined in e.g. [25] by:

$$\frac{1}{V_{tot}} \sum_i V_i \arccos\left(\frac{\boldsymbol{u}_i \cdot \nabla\theta_i}{\|\boldsymbol{u}_i\| \, \|\nabla\theta_i\|}\right),$$

Figures 11 and 12 depict the mean synergy angle versus the thermal power gain for the cases represented on the Pareto front from Figures 9 and 10. Two statements can be made from these plots.
First, even optimizing $(\mathcal{J}_1, \mathcal{J}_2)$ (reds points) increases the synergy field, it can be established that the mean synergy angle tends to decrease when the thermal power gain increases for those red points.
Secondly, a better field synergy doesn't automatically lead to a better heat transfer. Some green points over these plots show better synergy than some other points but with less heat exchanged. For example, for the single pipe we can see that the SP2 (green cross) has a mean synergy of 80% while SP1 (red cross) has a mean synergy field of 55% although both cases has nearly the same thermal power gain (see Table 2). This confirms the critic of Bejan [26] that a good synergy field doesn't automatically link to good heat transfer.

Even if these results are not presented, the same conclusion can be established for the other tested couple of Reynolds and Richardson numbers.

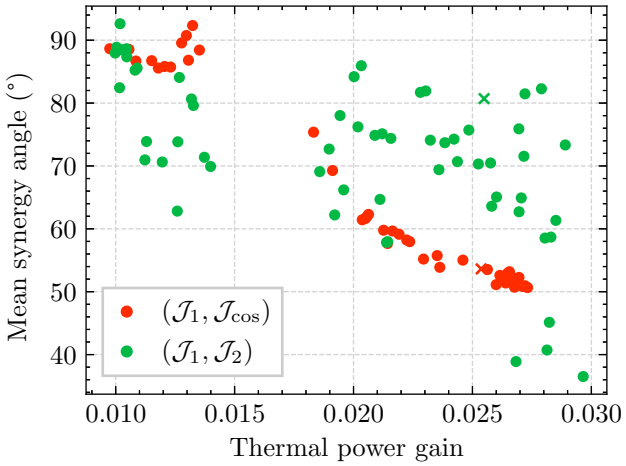

Figure 11: Mean synergy versus thermal power gain for the single pipe – Re=200 Ri=0.3

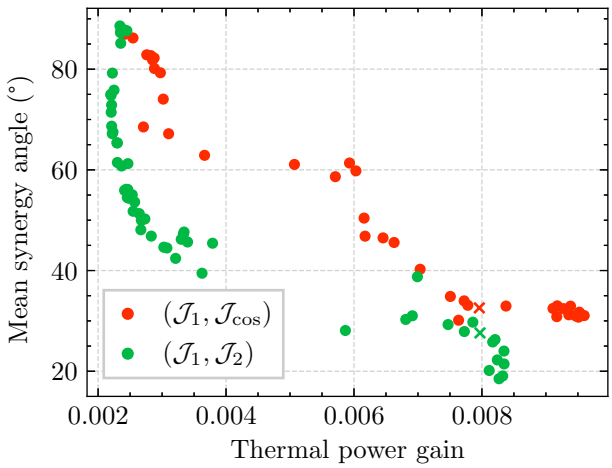

Figure 12: Mean synergy versus thermal power gain for the bend pipe – Re=200 Ri=0.3

6. Conclusions and perspectives

This paper used a topology optimization method for Newtonian laminar flow involving heat transfer. A new objective function involving the local angle between the velocity field and the temperature gradient has been proposed. This approach connects with the so-called field synergy principle (FSP). This objective function is tested along and compared with more classical ones in a multi-objective optimization process based on an adjoint solver. The single pipe and bend pipe configurations are studied with several Reynolds and Richardson numbers. The performance of the cosine objective function has been compared with the classical thermal power objective function with the use of Pareto front. The field synergy principle has been analyzed by comparing the mean field synergy angle to the thermal power gain between the inlet and outlet of the geometry.

The research findings of the present paper can be summarized as follows:

1. The proposed cosine objective function enhances the thermal transfer.
2. Compared to the classical approach, the cosine objective function leads to comparable performance. Sometimes, better performances are shown for the studied cases.
3. Improvement of the field synergy principle generally leads to better heat transfers.
4. High field synergy sometimes leads to less heat transfer than low field synergy, meaning that the field synergy principle is not always the best indicator of heat exchange through a domain.

Since a criticism of the FSP principle is that this principle is more advantageous near the heat exchange interfaces, further studies should design a cosine objective function involving only areas with some high gradient temperature to see if this could lead to a further increase of the heat exchange through a domain.

7. Acknowledgements

All the authors are supported by the "Agence Nationale de la Recherche" (ANR), Project O-TO-TT-FU number ANR-19-CE40-0011.

References

[1] R. L. Webb, N.-H. Kim, Principles of Enhanced Heat Transfer, Garland Science, 2004. URL: https://doi.org/10.1201/b12413. doi:10.1201/b12413.

[2] T. Borrvall, J. Petersson, Topology optimization of fluids in stokes flow, International Journal for Numerical Methods in Fluids 41 (2002) 77–107. URL: https://doi.org/10.1002/fld.426. doi:10.1002/fld.426.

[3] J. Alexandersen, C. S. Andreasen, A review of topology optimisation for fluid-based problems, Fluids 5 (2020) 29. URL: https://doi.org/10.3390/fluids5010029. doi:10.3390/fluids5010029.

[4] A. Fawaz, Y. Hua, S. Le Corre, Y. Fan, L. Luo, Topology optimization of heat exchangers: A review, Energy (2022) 124053.

[5] E. M. Dede, Multiphysics topology optimization of heat transfer and fluid flow systems, in: proceedings of the COMSOL Users Conference, volume 715, 2009.

[6] G. H. Yoon, Topological design of heat dissipating structure with forced convective heat transfer, Journal of Mechanical Science and Technology 24 (2010) 1225–1233. URL: https://doi.org/10.1007/s12206-010-0328-1. doi:10.1007/s12206-010-0328-1.

[7] J. Alexandersen, N. Aage, C. S. Andreasen, O. Sigmund, Topology optimisation for natural convection problems, International Journal for Numerical Methods in Fluids 76 (2014) 699–721. URL: https://doi.org/10.1002/fld.3954. doi:10.1002/fld.3954.

[8] G. Marck, M. Nemer, J.-L. Harion, Topology optimization of heat and mass transfer problems: Laminar flow, Numerical Heat Transfer, Part B: Fundamentals 63 (2013) 508–539. URL: https://doi.org/10.1080/10407790.2013.772001. doi:10.1080/10407790.2013.772001.

[9] D. Ramalingom, P.-H. Cocquet, A. Bastide, A new interpolation technique to deal with fluid-porous media interfaces for topology optimization of heat transfer, Computers & Fluids 168 (2018) 144–158. URL: https://doi.org/10.1016/j.compfluid.2018.04.005. doi:10.1016/j.compfluid.2018.04.005.

[10] M. Pietropaoli, F. Montomoli, A. Gaymann, Three-dimensional fluid topology optimization for heat transfer, Structural and Multidisciplinary Optimization 59 (2018) 801–812. URL: https://doi.org/10.1007/s00158-018-2102-4. doi:10.1007/s00158-018-2102-4.

[11] L. C. Høghøj, D. R. Nørhave, J. Alexandersen, O. Sigmund, C. S. Andreasen, Topology optimization of two fluid heat exchangers, International Journal of Heat and Mass Transfer 163 (2020) 120543. URL: https://doi.org/10.1016/j.ijheatmasstransfer.2020.120543. doi:10.1016/j.ijheatmasstransfer.2020.120543.

[12] D. Ramalingom, P.-H. Cocquet, R. Maleck, A. Bastide, A multi-objective optimization problem in mixed and natural convection for a vertical channel asymmetrically heated, Structural and Multidisciplinary Optimization 60 (2019) 2001–2020.

[13] A. Gersborg-Hansen, M. P. Bendsøe, O. Sigmund, Topology optimization of heat conduction problems using the finite volume method, Structural and Multidisciplinary Optimization 31 (2006) 251–259. URL: https://doi.org/10.1007/s00158-005-0584-3. doi:10.1007/s00158-005-0584-3.

[14] M. P. Bendsøe, O. Sigmund, Topology Optimization, Springer Berlin Heidelberg, Berlin ; New York, 2004. URL: https://doi.org/10.1007/978-3-662-05086-6. doi:10.1007/978-3-662-05086-6.

[15] Y. Tian, X. Liu, Q. Xu, Q. Luo, H. Zheng, C. Song, Z. Zhu, K. Gao, C. Dang, H. Wang, Y. Xuan, Bionic topology optimization of fins for rapid latent heat thermal energy storage, Applied Thermal Engineering 194 (2021) 117104. URL: https://doi.org/10.1016/j.applthermaleng.2021.117104. doi:10.1016/j.applthermaleng.2021.117104.

[16] X. Zhao, M. Zhou, O. Sigmund, C. S. Andreasen, A "poor man's approach" to topology optimization of cooling channels based on a Darcy flow model, International Journal of Heat and Mass Transfer 116 (2018) 1108–1123. URL: https://doi.org/10.1016/j.ijheatmasstransfer.2017.09.090. doi:10.1016/j.ijheatmasstransfer.2017.09.090.

[17] B. Zhang, Z. Jihong, G. Xiang, G. Limin, Design of nanofluid-cooled heat sink using topology optimization, Chinese Journal of Aeronautics 34 (2021) 301–317.

[18] S. Sun, P. Liebersbach, X. Qian, 3D topology optimization of heat sinks for liquid cooling, Applied Thermal Engineering 178 (2020) 115540. URL: https://doi.org/10.1016/j.applthermaleng.2020.115540. doi:10.1016/j.applthermaleng.2020.115540.

[19] H. Kobayashi, K. Yaji, S. Yamasaki, K. Fujita, Freeform winglet design of fin-and-tube heat exchangers guided by topology optimization, Applied Thermal Engineering 161 (2019) 114020. URL: https://doi.org/10.1016/j.applthermaleng.2019.114020. doi:10.1016/j.applthermaleng.2019.114020.

[20] H. Li, X. Ding, F. Meng, D. Jing, M. Xiong, Optimal design and thermal modelling for liquid-cooled heat sink based on multi-objective topology optimization: An experimental and numerical study, International Journal of Heat and Mass Transfer 144 (2019) 118638. URL: https://doi.org/10.1016/j.ijheatmasstransfer.2019.118638. doi:10.1016/j.ijheatmasstransfer.2019.118638.

[21] T. Van Oevelen, M. Baelmans, Application of topology optimization in a conjugate heat transfer problem, in: OPT-i 2014-1st International Conference on Engineering and Applied Sciences Optimization, Proceedings, 2014, pp. 562–577.

[22] S. Jia, X. Cao, X. Yuan, K.-T. Yu, Multi-objective topology optimization for the solar thermal decomposition of methane reactor enhancement, Chemical Engineering Science 231 (2021) 116265. URL: https://doi.org/10.1016/j.ces.2020.116265. doi:10.1016/j.ces.2020.116265.

[23] Q. Li, X. Yuan, P. Neveu, G. Flamant, L. Luo, A novel optimization approach to convective heat transfer enhancement for solar receiver, Chemical Engineering Science 116 (2014) 806–816. URL: https://doi.org/10.1016/j.ces.2014.05.051. doi:10.1016/j.ces.2014.05.051.

[24] Z. Guo, D. Li, B. Wang, A novel concept for convective heat transfer enhancement, International Journal of Heat and Mass Transfer 41 (1998) 2221–2225. URL: https://doi.org/10.1016/s0017-9310(97)00272-x. doi:10.1016/s0017-9310(97)00272-x.

[25] Z. Guo, W. Tao, R. Shah, The field synergy (coordination) principle and its applications in enhancing single phase convective heat transfer, International Journal of Heat and Mass Transfer 48 (2005) 1797–1807. URL: https://doi.org/10.1016/j.ijheatmasstransfer.2004.11.007. doi:10.1016/j.ijheatmasstransfer.2004.11.007.

[26] A. Bejan, Heatlines (1983) versus synergy (1998), International Journal of Heat and Mass Transfer 81 (2015) 654–658. URL: https://doi.org/10.1016/j.ijheatmasstransfer.2014.10.056. doi:10.1016/j.ijheatmasstransfer.2014.10.056.

[27] X. W. Zhu, J. Q. Zhao, Improvement in field synergy principle: More rigorous application, better results, International Journal of Heat and Mass Transfer 100 (2016) 347–354. URL: https://doi.org/10.1016/j.ijheatmasstransfer.2016.05.003. doi:10.1016/j.ijheatmasstransfer.2016.05.003.

[28] W.-Q. Tao, Y.-L. He, L. Chen, A comprehensive review and comparison on heatline concept and field synergy principle, International Journal of Heat and Mass Transfer 135 (2019) 436–459. URL: https://doi.org/10.1016/j.ijheatmasstransfer.2019.01.143. doi:10.1016/j.ijheatmasstransfer.2019.01.143.

[29] X. Zhao, J. E, Z. Zhang, J. Chen, G. Liao, F. Zhang, E. Leng, D. Han, W. Hu, A review on heat enhancement in thermal energy conversion and management using field synergy principle, Applied Energy 257 (2020) 113995. URL: https://doi.org/10.1016/j.apenergy.2019.113995. doi:10.1016/j.apenergy.2019.113995.

[30] Y. He, W. Tao, F. Song, W. Zhang, Three-dimensional numerical study of heat transfer characteristics of plain plate fin-and-tube heat exchangers from view point of field synergy principle, International Journal of Heat and Fluid Flow 26 (2005) 459–473. URL: https://doi.org/10.1016/

j.ijheatfluidflow.2004.11.003. doi:10.1016/j.ijheatfluidflow.2004.11.003.

[31] Y. Tao, Y. He, J. Huang, Z. Wu, W. Tao, Three-dimensional numerical study of wavy fin-and-tube heat exchangers and field synergy principle analysis, International Journal of Heat and Mass Transfer 50 (2007) 1163–1175. URL: https://doi.org/10.1016/j.ijheatmasstransfer.2006.03.019. doi:10.1016/j.ijheatmasstransfer.2006.03.019.

[32] Y. Tao, Y. He, Z. Wu, W. Tao, Three-dimensional numerical study and field synergy principle analysis of wavy fin heat exchangers with elliptic tubes, International Journal of Heat and Fluid Flow 28 (2007) 1531–1544. URL: https://doi.org/10.1016/j.ijheatfluidflow.2007.02.001. doi:10.1016/j.ijheatfluidflow.2007.02.001, revised and extended papers from the 5th conference in Turbulence, Heat and Mass Transfer.

[33] M. O. Hamid, B. Zhang, L. Yang, Application of field synergy principle for optimization fluid flow and convective heat transfer in a tube bundle of a pre-heater, Energy 76 (2014) 241–253. URL: https://doi.org/10.1016/j.energy.2014.06.055. doi:10.1016/j.energy.2014.06.055.

[34] Y. Zhai, Z. Li, H. Wang, J. Xu, Analysis of field synergy principle and the relationship between secondary flow and heat transfer in double-layered microchannels with cavities and ribs, International Journal of Heat and Mass Transfer 101 (2016) 190–197. URL: https://doi.org/10.1016/j.ijheatmasstransfer.2016.05.025. doi:10.1016/j.ijheatmasstransfer.2016.05.025.

[35] M. D. Gunzburger, Perspectives in Flow Control and Optimization, Society for Industrial and Applied Mathematics, 2002. URL: https://doi.org/10.1137/1.9780898718720. doi:10.1137/1.9780898718720.

[36] H. G. Weller, G. Tabor, H. Jasak, C. Fureby, A tensorial approach to computational continuum mechanics using object-oriented techniques, Computers in Physics 12 (1998) 620. URL: https://doi.org/10.1063/1.168744. doi:10.1063/1.168744.

[37] V. Subramaniam, T. Dbouk, J.-L. Harion, Topology optimization of conjugate heat transfer systems: A competition between heat transfer enhancement and pressure drop reduction, International Journal of Heat and Fluid Flow 75 (2019) 165–184. URL: https://doi.org/10.1016/j.ijheatfluidflow.2019.01.002. doi:10.1016/j.ijheatfluidflow.2019.01.002.